

Received December 12, 2018, accepted December 25, 2018, date of publication January 10, 2019, date of current version February 8, 2019.

Digital Object Identifier 10.1109/ACCESS.2019.2891532

# Design, Implementation and Control of an Improved Hybrid Pneumatic-Electric Actuator for Robot Arms

BEHRAD ROUZBEH<sup>ID</sup><sup>1</sup>, GARY M. BONE<sup>ID</sup><sup>1</sup>, GRAHAM ASHBY<sup>2</sup>, AND EUGENE LI<sup>1</sup>

<sup>1</sup>Department of Mechanical Engineering, McMaster University, Hamilton, ON L8S 4L7, Canada

<sup>2</sup>MANTECH, Inc., Guelph, ON N1H 6J2, Canada

Corresponding author: Gary M. Bone (gary@mcmaster.ca)

This work was supported by the Natural Sciences and Engineering Research Council of Canada (NSERC) through a Discovery Grant.

**ABSTRACT** Actuators used in robot arms need to be powerful, precise, and safe. We present the design, implementation, and control of a novel rotary hybrid pneumatic-electric actuator (HPEA) for use in robot arms, and collaborative robots in particular (also known as “cobot”). This HPEA is capable of producing torque 3.5 times larger than existing HPEA designs while maintaining low mechanical impedance (due to low values of friction and inertia) and inherent safety. The HPEA prototype has 450 times less inertia and 15 times less static friction in comparison to a conventional robot actuator with similar maximum continuous output torque. The HPEA combines the large slow torque generated by four pneumatic cylinders, connected to the output shaft via rack and pinion gears, with the small fast torque generated by a small DC motor directly connected to the output shaft. The direct connection of the motor avoids the higher cost and lower precision caused by a gearbox or harmonic drive. The control system consists of an outer position control loop and two inner pressure control loops. High precision position tracking control is achieved due to the combination of a model-based pressure controller, model-based position controller, adaptive friction compensator, and offline payload estimator. Experiments were performed with the actuator prototype rotating a link and payload in the vertical plane. Averaged over five tests, a root-mean-square error of 0.024° and a steady-state error (SSE) of 0.0045° were achieved for a fast multi-cycloidal trajectory. This SSE is almost ten times smaller than the best value reported for previous HPEAs. An offline payload estimation algorithm is used to improve the control system’s robustness. Finally, the superior safety of the HPEA is shown by modeling and simulating a constrained head-robot impact, and comparing the result with similar electric and pneumatic actuators.

**INDEX TERMS** Collaborative robots, hybrid pneumatic-electric actuator, impact modeling, pneumatic actuators, position control, robot control.

## I. INTRODUCTION

Robot arms need actuators with high continuous torque capacity and high precision. Electric motors are commonly used for driving robot joints as they are easy to control, and can achieve a fast and accurate response. Due to their relatively low torque-to-mass ratio, electric motors need to be coupled with high-ratio transmissions such as gearboxes or harmonic drives (typically with ratios of 100:1 or larger). Using a high-ratio transmission causes the actuator’s mechanical impedance to increase. This increase in impedance can then increase impact forces to dangerous levels. These impact forces are of particular concern with robots working in close proximity to humans (known as collaborative robotics), where high impact collisions may result

in injury. Furthermore, for high impedance actuators to achieve precise force control either expensive joint torque or tool force sensors are required.

The high impedance of the actuator is caused by two main sources. First, the moment of inertia at the gearbox output is equal to the motor’s inertia multiplied by the transmission ratio squared. With such large transmission ratios, even with small motor inertia, the moment of inertia at the output shaft becomes quite large. Secondly, the actuator’s friction torque is calculated by taking the friction torque of the motor multiplied by the transmission ratio and then adding the friction torque introduced by the transmission drive. Again, when large transmission ratios are used even small torques are significantly amplified. Another disadvantage of electric motors

is their tendency to overheat when providing large continuous torques, a common requirement during tasks where the robot arm is carrying a heavy payload. Compared to electric motors, pneumatic actuators are more cost effective, able to produce better power to weight ratios, avoid overheating and have naturally low impedance due to the inherent compliance of air. However, pneumatic actuators are unable to obtain the same level of fast and precise control that is possible with traditional electric motors.

A hybrid pneumatic-electric actuator (HPEA) can combine the advantages of both electric and pneumatic actuators, while mitigating their disadvantages. With a HPEA, the electric and pneumatic actuators may be connected in series or in parallel. Both series and parallel configurations produce lower impedance than the conventional motor plus high-ratio transmission electric actuator. Connecting them in series increases the speed and position control precision compared to a pneumatic actuator, but does not increase the power output. Connecting them in parallel improves the output power and power to weight ratio compared with an electric actuator; and the speed and position control precision compared to a pneumatic actuator. Furthermore, the large torque provided by the pneumatic actuator allows a low transmission ratio (or even no transmission) to be used with the motor, allowing the actuator's mechanical impedance to remain low. For these reasons, only parallel-connected HPEA will be considered in this paper. A HPEA is an embodiment of the DM<sup>2</sup> actuation approach proposed in [1]. In [1], the DM<sup>2</sup> advantages relative to series-elastic actuation (e.g., used by Baxter robot from ReThink Robotics) and joint torque controlled actuation (e.g., used by the Kuka LBR iiwa robot) are also explained.

Many position control algorithms have been investigated for pneumatic actuators, including sliding-mode control (SMC) [2]–[5] and [28], adaptive control [6]–[8], iterative learning control [9], backstepping [10], PID [11], and feedback linearization [27]. However, unlike pneumatic actuators, very limited research has been conducted on HPEAs.

An early concept for a rotary actuator combining a pneumatic actuator and electric motor was proposed in a patent from 1987 [12]. This design was created to solve the aforementioned overheating problem and provide the desired low power to weight ratio for high payload applications. As this design was never actually produced, we consider the HPEA designs from [13]–[20] to be the most relevant.

In [13], a DC motor was connected in parallel with a rotary pneumatic motor using a pair of gears. This motor was used to drive a single-link robot through a second set of gears attached to the output shaft. The gear ratio between the pneumatic actuator and the output shaft was 30:1, and the 15:1 between the electric motor and the output shaft. The pneumatic torque was controlled using two servo valves, and two pressure sensors. The angle of the output shaft was measured with an optical encoder. Two different control algorithms were studied. A sinusoidal position trajectory was tracked using a SMC strategy. This SMC strategy made use of

a linearized model of the hybrid actuator. For point-to-point motion control, a mixture of the SMC strategy and a simple PD control was implemented. Experimental results for different horizontal motions were included for: step inputs, and a 200° peak-to-peak, 0.5 Hz, sine wave trajectory. In comparison to the pneumatic actuator with SMC control, the HPEA was able to reduce the settling time of the system from 1.2 s to 0.5 s for the step input, and reduce the maximum following error from 20° (10%) to less than 10° (5%) for the sine wave trajectory.

The HPEA prototypes described in [14], [16], and [18] included one or two pneumatic muscle actuators (PMAs) connected by cable(s) to an output pulley, along with a DC motor connected to the output pulley by a gearbox. In [14] a 0.0305 m radius pulley was used with a gearbox with a 28:1 reduction ratio. The PMA pressure was controlled using a proportional valve and a simple PID controller. The angular position of the joint was controlled using acceleration feedforward plus PD controller. This work included experimental results for 12° peak-to-peak, 1 Hz and 3 Hz sine wave position trajectories. The experimental results showed that the HPEA reduced the maximum following error from approximately 50% to about 10%, compared with the PMAs operating alone. In [16] a single PMA was controlled using a model-based plus PI controller, while a feedforward torque controller was used to control the DC motor. Experimental results were presented for 190° step change and 30° peak-to-peak 2 Hz sinusoidal position trajectories. For the step change the steady-state error (SSE) was 3.4° (11%). For the sinusoidal trajectory the maximum tracking error was about 9° (30%). A two-stage optimal control strategy for a PMA plus DC motor was proposed in [18]. Their strategy first solved for the optimal motor and PMA inputs using a long term prediction horizon with a coarse time resolution. In the 2<sup>nd</sup> stage, the input for the motor was re-optimized using a shorter prediction horizon with a finer time resolution. Experimental results were presented for 1.2 rad peak-to-peak, 0.25 Hz and 1.0 Hz sinusoidal trajectories. For 1.0 Hz vertical motions with no payload, the root mean square error (RMSE) values for the PMA alone and the HPEA were 0.24 rad and 0.075 rad, respectively.

A unique design for a linear HPEA was presented in [17]. Their design integrates a pneumatic cylinder and a linear electric motor into a very compact device. They controlled the forces produced by the cylinder and motor using separate PI controllers. The HPEA reduced the force RMSE to 1.77 N compared to the 6.26 N obtained using only the pneumatic cylinder. They did not control the HPEA's position or use it to drive a rotary joint.

The HPEA proposed in [15] and [19] generated most of its torque through a single pneumatic cylinder. This cylinder was used to both push and pull a rack gear that meshed with a pinion gear directly connected to the output shaft. The remainder of the torque was generated by a DC motor which drove the same pinion via a smaller gear (giving a 5:1 ratio). Instead of controlling the on/off solenoid valves with

pulse-width modulation (PWM), the valves were switched on/off by a discrete-valued model predictive control algorithm. The electric motor was controlled using a form of inverse dynamics control. Bone *et al.* [19] reported improved position control results using these methods. In their experiments, the actuators rotated loads in the vertical plane from  $0^\circ$  to  $90^\circ$  following a cycloidal trajectory; where  $90^\circ$  corresponded to the maximum gravity load. With only the pneumatic actuator, the RMSE and SSE from these experiments were  $0.64^\circ$  and  $0.23^\circ$ , respectively. With the HPEA the RMSE and SSE were reduced to  $0.11^\circ$  and  $0.04^\circ$ , respectively.

This paper is an extended and improved version of our previous conference paper [20]. It also builds upon our pneumatic actuator controller from [27] and uses our electric-actuated robot impact model from [22].

The contributions of this paper are as follows:

1. A new HPEA design that produces higher torque than all previous designs, avoids the cost and lower precision caused by a gearbox (or harmonic drive).
2. Using model-based pressure control [27] with the HPEA rather than the PI control used in [20].
3. A high precision position controller has been developed that provides robustness to unknown payloads and friction uncertainty.
4. Robust stability analysis of the HPEA including the inner-loop pressure controllers and outer-loop position controller (not included in [20]).
5. Dynamic models for constrained impacts between a human's head and a robot arm are developed and simulated for electric, pneumatic and hybrid actuated robotic arms.
6. Experimental results demonstrating superior position tracking performance compared to [20] and [27] and the best results from the literature.

In section II, the design's advancements are compared to previous designs, and the implementation details of the prototype are described. This is followed by a quantitative comparison of the new HPEA to prior HPEAs, along with a conventional robot actuator in section III. The system model and control algorithm are then presented in sections IV and V, respectively. The payload estimator is described in section VI. The human-robot impact models and simulation results are given in section VII. Finally, experimental results and conclusions are presented in sections VIII and IX, respectively.

## II. MECHATRONIC DESIGN AND IMPLEMENTATION OF THE HYBRID PNEUMATIC-ELECTRIC ACTUATOR

The new HPEA design introduces several advancements over previous HPEA design approaches. First, the electric motor is directly attached to the output shaft rather than being connected via gears as in [13]–[16], [18], and [19]. By eliminating these gears, the associated friction and backlash from the gears are also eliminated. Furthermore, by directly coupling the motor to the output shaft, the amplification of mechanical impedance caused by a gearbox (as discussed in section I) is also avoided.

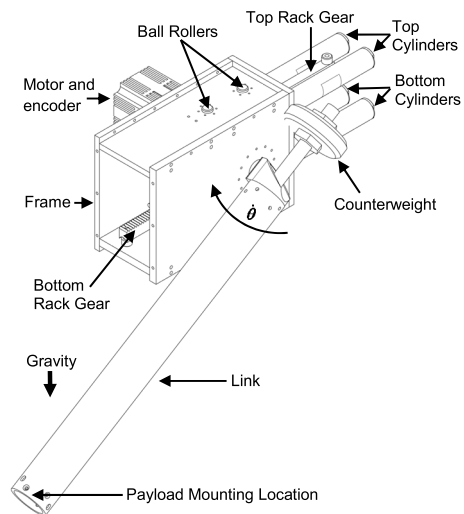


**FIGURE 1.** Assembly drawing of the rotary hybrid actuator.

Second, we are able to directly measure the output shaft's angle, instead of inferring it from the piston position, or from a geared encoder as was done in [15] and [19]. By directly measuring the angle we are able to obtain more precise position control. This stems from the fact that all errors caused by the gears between the sensor and output shaft have been eliminated.

Third, the power generated by the pneumatic actuator is transmitted with a pair of rack gears that are meshed with a single pinion coupled to the output shaft. This approach allows the extension and retraction forces from the pneumatic actuator to be used, rather than only the retraction forces, as is the case with a belt-pulley or cable-pulley transmission [14], [16], [18]. This however comes with the tradeoff that it is less compact than those previous designs. In the proposed design, the rack gears are located above and below the pinion, reducing the loading on the output shaft and its support bearings, compared with the single rack design utilized in [15] and [19].

Fourth, low friction pneumatic cylinders were chosen over rotary pneumatic motors [13] or PMAs [14], [16], [18]. Rotary pneumatic motors suffer from large friction torques caused by their seals, while PMAs suffer from friction induced hysteresis and a displacement dependent output force [23]. By using low friction pneumatic cylinders, both disadvantages were avoided; making precise position control easier and reducing the energy lost to friction.

The design details of the HPEA assembly can be seen in Fig. 1. As the drawing shows, the actuator has a top and bottom rack gear, each controlled with a pair of pneumatic cylinders on the corresponding top and bottom. These cylinders are located to the left and right of each of the rack gears. This configuration allows a compact arrangement, since the racks are able to travel in between the pairs of cylinders. Furthermore, the arrangement applies zero net moment to the racks when the cylinder pairs push or pull together.

A novel approach is used to guide each of the rack gears. First, a semicircular groove was machined into the back of each gear. Second, a pair of ball rollers are located such that their balls roll in each groove. This allows the minimum constraint for proper meshing to occur, without binding the assembly. Furthermore, the preload force at each of the ball rollers can be adjusted, to allow the backlash between the rack and pinion gears to be tuned and minimized. As can also be seen in the figure, the pinion gear is mounted on the output shaft. This output shaft can be connected to a rigid robot link to provide rotational motion. A counterweight is also added to the output shaft to balance the torque due to gravity from the mass of the link. The link angle  $\theta$ , is defined as zero when the link is pointing vertically downwards and positive in the clockwise direction.

The stroke of the cylinder, and the pitch ratio of the pinion are key HPEA design parameters. Both parameters influence the output torque, the range of rotary motion, and the size of the actuator. A larger cylinder stroke will increase the range of motion, but will also increase the actuator size. A larger pitch radius increases the output torque, but decreases the range of motion, as well as increasing the actuator size. In our design we chose a design constraint of  $180^\circ$  as the minimum range of motion. This was chosen as it was considered enough motion for either a shoulder or elbow joint in a robot. A value of 40 Nm was chosen as the target for the maximum continuous output torque. This value was selected to ensure the actuator was comparable to the rated continuous joint torque of a small industrial robot (e.g. Universal Robots UR3 [24] or CRS A465 [25]). These design specifications are achieved in our implementation using four low friction cylinders with a 27 mm bore and 152 mm stroke (SMC, model NCMB106); and a stainless-steel pinion with a 31.5 mm pitch radius.

The optimal ratio of maximum electric motor torque to maximum total HPEA torque is an open problem. The motor should generate enough torque to compensate for the deficiencies of the pneumatic actuator, but should still be small enough that it does not increase the HPEA size or mass significantly. The motor should also have a low inertia rotor to keep the HPEA's overall mechanical impedance low, but as stated before, this typically comes at the expense of reduced torque. For the proposed design, a small brushless DC motor was selected (Animatics, model SM3430D, in current control mode). This motor is capable of a peak torque of 3.25 Nm, a continuous torque of 1.09 Nm, and has a  $1.34 \times 10^{-4}$  kgm<sup>2</sup> rotor inertia. The angle of the output shaft is obtained with a high-resolution encoder mounted on the motor's rear shaft (Quantum Devices, model QR12-20000, giving  $8 \times 10^4$  counts/rev using quadrature counting). Since the motor is directly coupled to the output shaft, the resolution of the position measurement is  $0.0045^\circ$ .

Fig. 2 presents a schematic diagram for the pneumatic, electrical and mechanical components of the HPEA. Based on the assembly of the racks and cylinders, the top cylin-

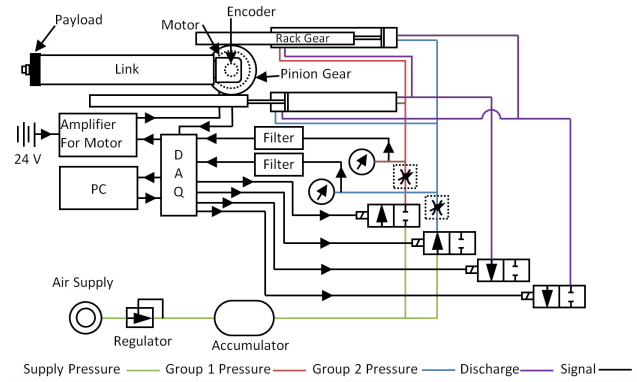


**FIGURE 2.** Schematic diagram of the pneumatic, electrical and mechanical components of the hybrid actuator.

ders' chambers containing rods and the bottom cylinders' chambers without rods, work together to form what we term "Chamber Group 1" (CG1). Similarly, "Chamber Group 2" (CG2), is made up of the top cylinders' chambers without rods and the bottom cylinders' chambers containing rods (i.e. the opposite of CG1).

The area of both chamber groups is equal to four times the bore's cross-sectional area, minus two times the rod's cross-sectional area. Furthermore, CG1 drives the output shaft in the positive direction when its pressure is greater than CG2, with CG2 driving the shaft in reverse when the opposite is true.

Simple on/off solenoid valves were chosen, as they are considerably less expensive than proportional/servo valves (\$40 USD vs. \$800 USD). PWM was utilized to approximate the flow behavior of a proportional/servo valve, as was done in [3], [5], and [11]. To allow each CG's pressure to be controlled independently two high speed 2/2 solenoid valves (FESTO MHJ10) are connected to each CG, i.e. one valve is used for charging and other for discharging the CG. To attenuate high frequency noise, the pressure sensor outputs (SSI Model P51-100) were passed through low pass filters with a 95 Hz cut off frequency. The pressure and position measurements are obtained using a National Instruments (NI) data acquisition system (DAQ). The DAQ (NI, models PCIe-6353 and PCI-6602) samples the sensors at 1 kHz and outputs the PWM signals to the valve drivers. The control algorithms are implemented in C language on a PC containing an Intel Core i5 2400 (3.1 GHz) processor. A photograph of the finished prototype is shown in Fig. 3.

### III. COMPARISON OF NEW HPEA TO PRIOR HPEAS AND A CONVENTIONAL ROBOT ACTUATOR

The specifications of the new HPEA design were compared to those for previous HPEAs and for a conventional robot actuator. The results are listed in Table 1. The ratios of motor torque to total torque were calculated using the maximum continuous torque values. Also note that several of the specifications are underestimated as explained in the table's footnotes.

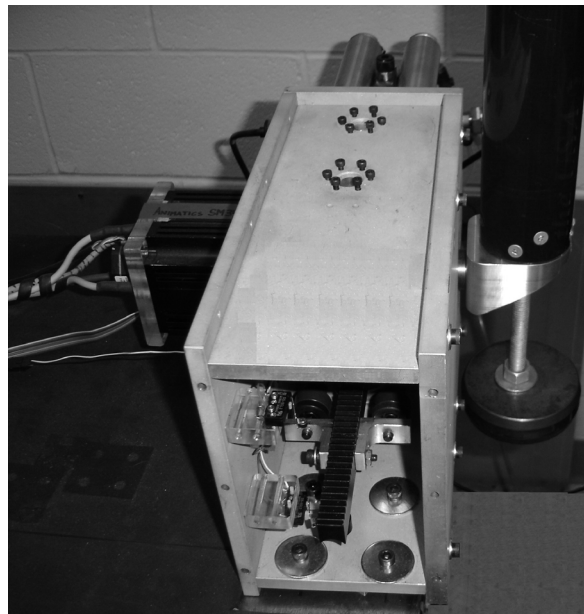


**FIGURE 3.** Photograph of the hybrid actuator with the link at  $\theta=180^\circ$ .

**TABLE 1.** Comparison of HPEA and DC motor plus harmonic drive actuator specifications.

Spec.	Robot Actuator				
	HPEA from [13]	HPEA from [14]	HPEA from [15][19]	New HPEA	DC motor + HDT <sup>a</sup> [25][26]
Max. cont. torque (Nm)	10.9	7.1	10.0 <sup>b</sup>	37.7 <sup>b</sup>	39.5
Ratio of motor torque to total torque (%)	14	14	10	3	100
Static friction torque at output shaft (Nm)	> 9.7 <sup>c</sup>	n/a <sup>d</sup>	0.1	0.23	>3.4 <sup>e</sup>
Moment of inertia at output shaft (kgm <sup>2</sup> )	>1.5×10 <sup>-3</sup> <sup>f</sup>	>9.1×10 <sup>-4</sup> <sup>g</sup>	6.4×10 <sup>-5</sup>	2.0×10 <sup>-3</sup>	0.90

a. Used for CRS A465 robot arm joints 1 and 3. Equal to motor inertia ( $9.0 \times 10^{-5}$  kgm<sup>2</sup>) times transmission ratio (100) squared.

b. For 700 kPa absolute supply pressure.

c. Due to a lack of information in [13] this value does not include the friction torques from the DC motor, gears and bearings.

d. The information in [14] was insufficient to estimate the static friction torque.

e. This value does not include the unknown friction torques from the harmonic drive and the joint's bearings.

f. Due to a lack of information in [13] this value only includes the inertia of the DC motor.

g. Due to a lack of information in [14] this value only includes the inertia of the DC motor.

Based on the Table 1 data, the new HPEA design is capable of producing 3.5 more times continuous torque and is subject to 40 times less friction in comparison to the HPEA design in [13]. The new design also produces 5.4 times more torque than the design from [14]. The closest competitor is the HPEA from [15], [19], with the new design producing 3.77 times more torque. However, the new design does suffer from 2.3 times more friction, and 31 times higher inertia in comparison to the design in [15] and [19].

The new HPEA design is also able to achieve significantly more precise movement compared to previous designs.

These findings are detailed in section VIII. Lastly, the new HPEA design is able to achieve this with a ratio of motor torque to total torque of only 3%. This value is significantly smaller than previous HPEA designs. As discussed in section II, the motor torque is only required to compensate for the short comings in the response time and precision of the pneumatic actuator. We chose a smaller motor under the assumption that the torque from the pneumatic cylinders will be accurately controlled; therefore the electric motor is only required to make minor torque contributions. This assumption is validated by the experimental results presented in section VIII.

The most common actuator used by industrial robots is a DC motor connected to a harmonic drive transmission (HDT). To present a reasonable comparison, the proposed HPEA design is compared to a DC motor with a 100:1 HDT whose continuous rated torque is similar to the new HPEA. This motor plus HDT are used in joints 1 and 3 of the CRS A465 robot. This actuator was also chosen since its inertia and friction values can be estimated from the specifications of its CMC model 3515 motor [25], [26]. While the specifications of the actuators show that their torques are similar, the DC motor plus HDT have a moment of inertia that is 450 times larger than the proposed HPEA design. Furthermore, the static friction of the DC motor plus HDT is 15 times greater than that of the HPEA actuator. Given the significantly lower inertia, and lower static friction, we can conclude that the new HPEA design has much lower mechanical impedance than the conventional actuators used in robot arms. This lower impedance will lead to smaller collision forces when human-robot impacts occur. This safety issue will be investigated in section VII.

#### IV. SYSTEM MODELING

In this section we will introduce the system model that will be used to control the HPEA actuator. The system is comprised of two solenoid valves, four pneumatic cylinders, rack and pinion gears, an amplifier, a DC motor, a counterweight, rigid link and a payload mass. The rotational dynamics are defined by:

$$I_{total}\ddot{\theta} = \tau_m + \tau_p - \tau_g - \tau_f \quad (1)$$

where  $I_{total}$  is the total moment of inertia;  $\ddot{\theta}$  is the angular acceleration of the output shaft;  $\tau_p$  is the torque produced by the pneumatic cylinders;  $\tau_m$  is torque output of the motor;  $\tau_g$  is torque due to gravity acting on the payload, link and counterweight; and  $\tau_f$  is the friction torque. Note that  $I_{total}$  is the total moment of inertia including the payload mass, link, counterweight, pinion gear, rack gears, and various minor components. Recalling the CGs defined in section II, the pneumatic torque is given by:

$$\tau_p = r_p A_g (P_1 - P_2) \quad (2)$$

where  $r_p$  is the pinion gear's pitch radius;  $A_g = 4A_p - 2A_r$  is the total cross-sectional area of each CG;  $A_p$  and  $A_r$  are the cross-sectional areas of the each cylinder's piston and

rod, respectively;  $P_1$  and  $P_2$  are the pressures inside CG1 and CG2, respectively. Employing the ideal gas law, conservation of mass, and conservation of energy for each CG, the pressure dynamic equation for each chamber group is:

$$V_j \dot{P}_j + k P_j \dot{V}_j = \dot{m}_j kRT \quad j \in \{1, 2\} \quad (3)$$

where  $\dot{m}_j$  is the overall mass flow rate into the  $j^{\text{th}}$  CG,  $k$  is the ratio of specific heats for air (1.4),  $R$  is the universal gas constant ( $287 \text{ Pa} \cdot \text{m}^3 \cdot \text{K}^{-1}$ ),  $T$  is the air temperature,  $V_j$  is the CG volume, and  $P_j$  is the CG pressure. The time derivative of mass flow rate can be derived from (3) as:

$$\ddot{m}_j = (k P_j \ddot{V}_j + \dot{P}_j V_j + (1+k) \dot{P}_j \dot{V}_j) / kRT \quad j \in \{1, 2\} \quad (4)$$

The mass flow rate into each CG is dependent on the flow through the PWM driven supply and the discharge valves. Assuming the supply pressure ( $P_s$ ) and atmospheric pressure ( $P_0$ ) remain constant, the relationships between the mass flow rates into the CGs and the valve inputs are defined by (5).

$$\dot{m}_j = f_j(u_j, P_j) \quad j \in \{1, 2\} \quad (5)$$

In (5),  $u_j$  is the PWM duty cycle for the supply valve of the associated CG. The duty cycle for the discharge valve of each CG is simply defined as:  $1 - u_j$ . The functions  $f_1$  and  $f_2$  depend on the valve's internal geometry and are highly nonlinear. Combining (3) and (5), the pressure derivative model for each CG in (6) is obtained.

$$\dot{P}_j = (f_j(u_j, P_j) kRT - k P_j \dot{V}_j) / V_j \quad j \in \{1, 2\} \quad (6)$$

where:

$$\begin{cases} V_1 = V_{01} + A_g r_p \theta \\ V_2 = V_{02} - A_g r_p \theta \end{cases} \quad (7)$$

In (7),  $V_{01}$  and  $V_{02}$  are the CG1 and CG2 volumes at  $\theta = 0$ , respectively.

Since finding an accurate friction model is very difficult, if not impossible, a simple model is considered for the friction torque which will form the basis of implementing the adaptive friction compensator. This will be described in section V. Equation (8) shows the simple friction model.

$$\tau_f = \begin{cases} \tau_f^+ & \dot{\theta} > 0 \\ 0 & \dot{\theta} = 0 \\ \tau_f^- & \dot{\theta} < 0 \end{cases} \quad (8)$$

The motor dynamics are much simpler than the dynamics of the pneumatic actuator. The torque from the electric motor can be modelled as:

$$\tau_m = f_m(u_m) \quad (9)$$

where  $u_m$  is the command signal sent to the amplifier, and  $f_m(\cdot)$  is a nonlinear function. This function can be identified by calibration tests.

As mentioned in Section II, the counterweight balances the gravity torque acting on the link. Thus the remaining gravity torque is:

$$\tau_g = d_p m_p g \sin(\theta) \quad (10)$$

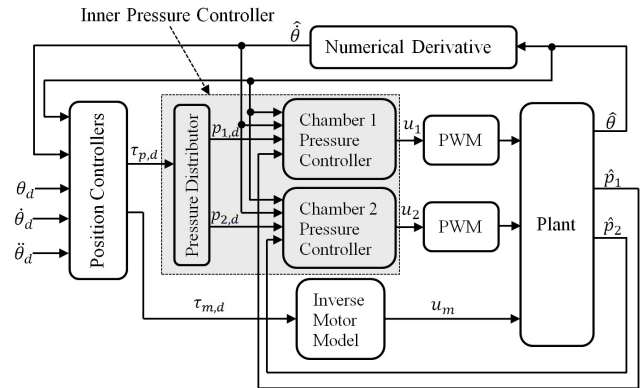


**FIGURE 4.** Overall control system structure.

where  $m_p$  is the mass of the payload attached to the end of the link, and  $d_p$  is the distance from the axis of rotation to the payload's center of mass. To draw a comparison between the rotary HPEA and a linear actuator, the mass equivalent to  $I_{total}$  can be calculated with:

$$m_{eq} = \frac{F}{\ddot{y}_b} = \frac{\tau / r_p}{r_p \ddot{\theta}} = \frac{I_{total} \ddot{\theta} / r_p}{r_p \ddot{\theta}} = \frac{I_{total}}{r_p^2} \quad (11)$$

## V. CONTROLLER DESIGN

The control system manipulates the duty cycles of the valves and the motor current to control the motion of the arm. The system requires four controllers to be designed: two inner-loop pressure controllers for CG1 and CG2; and two position controllers for the pneumatic actuator and the electric motor that form the outer-loop. Fig. 4 shows the structure of the overall control system.

### A. MODEL-BASED POSITION CONTROLLER FOR THE PNEUMATIC ACTUATOR

For position control of the pneumatic actuator we employed our model-based control law from [27]. It will be briefly summarized in this section. The control law includes feedforward terms based on (1), (2), (8) and (10). These feedforward terms provide a rapid response, while the feedback terms provide robustness. The desired torque from the pneumatic actuator is then:

$$\tau_{p,d}(t_i) = \hat{I}_{total} \ddot{\theta}_d(t_i) + \hat{\tau}_g(t_i) + \tau_f^*(t_i) - K_p \hat{e}_\theta - K_D \hat{e}_{\dot{\theta}} \quad (12)$$

where  $t_i = iT_s, i \in Z^+$  is the time of the current sample;  $\hat{I}_{total} \ddot{\theta}_d(t_i)$ ,  $\hat{\tau}_g(t_i)$  and  $\tau_f^*(t_i)$  are the inertia, gravity and adaptive friction compensation terms, respectively;  $\hat{e}_\theta = \hat{\theta}(t_i) - \theta_d(t_i)$  is the position error,  $\hat{e}_{\dot{\theta}} = \hat{\dot{\theta}}(t_i) - \dot{\theta}_d(t_i)$  is the velocity error,  $\hat{\theta}(t_i)$  is the sensed position;  $\hat{\dot{\theta}}(t_i)$  is the estimated velocity;  $K_p$  is the positive proportional gain,  $K_D$  is the positive derivative gain, and the symbol “^” denotes the measured or estimated value for the variable.  $\hat{\theta}(t_i)$  is estimated by backward differencing and low-pass filtering the sensed position. The adaptive friction compensator is defined by (13). In this equation,  $\tau_f^+, \tau_f^-$  are the values from the

friction model shown in (8); and  $\lambda^+$  and  $\lambda^-$  are the adaptation increments. Also  $\tau_{f,min}^*$ , and  $\tau_{f,max}^*$  are the lower and upper limits for the friction torque adaptation, respectively. When the desired velocity is zero,  $\tau_f^*(t_i)$  is adjusted until the position error magnitude is less than the threshold  $\delta$ . Note that in (13)  $\dot{\theta}_d(t_i)$  is used instead of  $\dot{\theta}(t_i)$  to avoid the detrimental effects of a noisy velocity estimate, especially near  $\dot{\theta} = 0$ .

$$\tau_f^*(t_i) = \begin{cases} \tau_f^+ & \dot{\theta}_d(t_i) > 0 \\ \tau_f^- & \dot{\theta}_d(t_i) < 0 \\ \tau_f^*(t_{i-1}) - \lambda^+ & \dot{\theta}_d(t_i) = 0 \wedge \hat{e}_\theta(t_i) > \delta \\ & \wedge \tau_f^*(t_{i-1}) > \tau_{f,min}^* \\ \tau_f^*(t_{i-1}) + \lambda^- & \dot{\theta}_d(t_i) = 0 \wedge \hat{e}_\theta(t_i) < -\delta \\ & \wedge \tau_f^*(t_{i-1}) < \tau_{f,max}^* \\ \tau_f^*(t_{i-1}) & \text{Otherwise} \end{cases} \quad (13)$$

The desired chamber pressures are given by:

$$P_{1,d}(t_i) = \frac{1}{2} (P_0 + P_s + \Delta P_d(t_i)), \quad (14)$$

$$P_{2,d}(t_i) = \frac{1}{2} (P_0 + P_s - \Delta P_d(t_i)) \quad \text{and} \quad (15)$$

$$\Delta P_d(t_i) = \tau_{p,d}(t_i)/(A_g r_p) \quad (16)$$

Equations (14)-(16) are designed to keep the CG pressures well above atmospheric since we have observed that the resulting higher air density improves the position tracking performance.

## B. POSITION CONTROLLER FOR THE ELECTRIC ACTUATOR

The electric motor improves the powerful but relatively slow pneumatically generated torque by adding smaller, high-frequency torques according to its position control law. A standard PD controller is effective for this application due to the simple dynamics of the electric motor. The control law is given by (17). Recalling (9), here an inverse motor calibration is performed to find function  $f'_m(\cdot)$  needed to calculate the motor input,  $u_m$ , as shown by equation (18).

$$\tau_{m,d}(t_i) = -K_{p,m}\hat{e}_\theta - K_{D,m}\hat{e}_{\dot{\theta}} \quad (17)$$

$$u_m = f'_m(\tau_{m,d}) \quad (18)$$

## C. INVERSE VALVE MODELS

Inverse valve models are required to implement the model-based pressure controller. Typically this involves fitting a forward valve model, that is either linear or quadratic in  $u$ , and then solving it for the unknown  $u$  using the known values: desired mass flow rate, measured chamber pressure, volume and volume time derivatives [3], [6], [10]. Inverse valve models have also been developed, e.g. using neural networks [21].

To avoid over simplifying the forward model to make it invertible, and also avoid the training difficulties (e.g., data hungry, local minima and overfitting) associated with neural networks, we employ the approach presented in [27].

With this approach the inverse behavior of each valve is modelled by a polynomial in three variables as follows:

$$\begin{cases} u_1(t_i) = f_{1,inv} \left( \hat{m}_{1d}(t_i), \hat{m}_{1d}(t_i), \hat{P}_1(t_i) \right) \\ u_2(t_i) = f_{2,inv} \left( \hat{m}_{2d}(t_i), \hat{m}_{2d}(t_i), \hat{P}_2(t_i) \right) \end{cases} \quad (19)$$

and

$$\begin{cases} f_{1,inv} = \sum_{\alpha=0}^A \sum_{\beta=0}^B \sum_{\gamma=0}^G C_{\alpha,\beta,\gamma} \hat{m}_{1d}(t_i)^\alpha \hat{m}_{1d}(t_i)^\beta \hat{P}_1(t_i)^\gamma \\ f_{2,inv} = \sum_{\alpha=0}^A \sum_{\beta=0}^B \sum_{\gamma=0}^G C_{\alpha,\beta,\gamma} \hat{m}_{2d}(t_i)^\alpha \hat{m}_{2d}(t_i)^\beta \hat{P}_2(t_i)^\gamma \end{cases} \quad (20)$$

where  $\hat{P}$  are the sensed pressures,  $\hat{m}_d$  are the desired mass flow rates and  $\hat{m}_d$  are the desired mass flow rate time derivatives for the CGs. The inclusion of  $\hat{m}_d$  in (20) was found to improve the fit of the model when rapid changes in  $\dot{m}$  occurred. The optimal coefficients  $C_{\alpha,\beta,\gamma}$  may be found by linear regression, avoiding the possibility of local minima.

## D. MODEL-BASED PRESSURE CONTROLLER

Each CG pressure will be controlled using the model-based control law we employed in [27]. Its equations are briefly summarized here, as follows:

$$\tilde{P}(t_i) = \dot{P}_d(t_i) - K'_P \hat{e}_P(t_i) - K_I \hat{E}_P(t_i) \quad (21)$$

$$\hat{m}_d(t_i) = \left( k \hat{P}(t_i) \hat{V}(t_i) + \tilde{P}(t_i) \hat{V}(t_i) \right) / kRT \quad (22)$$

$$\hat{m}_d(t_i) = \left( k \hat{P}(t_i) \hat{V}(t_i) + \ddot{P}_d(t_i) \hat{V}(t_i) + (1+k) \tilde{P}(t_i) \hat{V}(t_i) \right) / kRT \quad (23)$$

where  $\hat{e}_P(t_i) = \hat{P}(t_i) - P_d(t_i)$  is the pressure error;  $\hat{E}_P = \int_0^t \hat{e}_P dt$ ;  $K'_P$  and  $K_I$  are positive proportional and integral gains, respectively. Note that  $\hat{E}_P(t_i)$  is bounded to avoid integral windup. The valve duty cycles are calculated by substituting the values from (22) and (23), and the sensed pressures, into (19).

## E. ANALYSIS OF ROBUST STABILITY

To prove the robust stability of the HPEA's position control system it is first necessary to prove the robust stability of the inner-loop pressure control subsystems. In [27] it was proven that the pressure control subsystems for a rotary pneumatic actuator are bounded-input bounded-output stable when the model uncertainties are bounded. Since the dynamics of those subsystems are unchanged with the HPEA, the proof in [27] applies to them as well.

With the outer-loop position control system, the addition of the motor's torque requires that the stability proof from [27] be extended for the HPEA. Defining  $\Delta\tau_p = \tau_p - \tau_{p,d}$  as the pneumatic torque uncertainty, substitution into (2) gives:

$$\begin{aligned} \Delta\tau_p &= (P_1 - P_2)A_g r_p - (P_{1,d} - P_{2,d})A_g r_p \\ &= (e_{p,1} - e_{p,2})A_g r_p \end{aligned} \quad (24)$$

Equation (24) shows that  $\Delta\tau_p$  is also bounded. Similarly for the electric actuator, electric torque uncertainty is defined as

$\Delta\tau_m = \tau_m - \tau_{m,d}$ . Substituting (9) and (18) into the definition of  $\Delta\tau_m$  gives:

$$\Delta\tau_m = f_m(u_m) - \tau_{m,d} = f_m(f'_m(\tau_{m,d})) - \tau_{m,d} \quad (25)$$

With proper motor calibration, the estimated functions  $f_m$  and  $f'_m$  will nearly cancel out each other so  $\Delta\tau_m$  will be a small bounded value. Re-writing (12) gives:

$$\tau_p = \hat{I}_{total}\ddot{\theta}_d + \hat{\tau}_g + \tau_f^* - K_P(\hat{e}_\theta) - K_d(\dot{\hat{e}}_\theta) + \Delta\tau_p \quad (26)$$

The remaining bounded uncertainties are defined by  $\Delta\theta = \hat{\theta} - \theta$ ,  $\Delta\dot{\theta} = \hat{\dot{\theta}} - \dot{\theta}$ ,  $\Delta I_{total} = \hat{I}_{total} - I_{total}$ ,  $\Delta\tau_g = \hat{\tau}_g - \tau_g$ , and  $\Delta\tau_f = \tau_f^* - \tau_f$ . Substituting  $\tau_p$  from (1) into (26) gives:

$$\begin{aligned} I_{total}\ddot{\theta}_d + K_D\dot{\theta}_d + K_P e_\theta \\ = \Delta\tau_p + \Delta I_{total}\ddot{\theta}_d + \Delta\tau_f + \Delta\tau_g + \tau_m - K_P\Delta\theta - K_d\Delta\dot{\theta} \end{aligned} \quad (27)$$

Now substituting from (17) into (27), gives (28) and (29).

$$I_{total}\ddot{\theta}_d + (K_d + K_{D,m})\dot{\theta}_d + (K_P + K_{P,m})e_\theta = \Delta U_2 \quad (28)$$

$$\begin{aligned} \Delta U_2 = \Delta\tau_p + \Delta\tau_m + \Delta I_{total}\ddot{\theta}_d + \Delta\tau_f + \Delta\tau_g \\ - (K_P + K_{P,m})\Delta\theta - (K_d + K_{D,m})\Delta\dot{\theta} \end{aligned} \quad (29)$$

The total uncertainty  $\Delta U_2$  is made up of bounded terms so it is also bounded. Since  $I_{total} > 0$ ,  $K_d + K_{D,M} > 0$ , and  $K_P + K_{P,m} > 0$ , (28) guarantees that  $e_\theta$  converges inside a bounded region when inputs  $\theta_d$ ,  $\dot{\theta}_d$ , and  $\ddot{\theta}_d$  are bounded. So the HPEA's position control system is bounded-input bounded-output stable.

## VI. OFFLINE PAYLOAD ESTIMATION

Uncertainties in system dynamics are known to negatively affect the performance of model-based controllers. The proposed position controller uses the adaptive friction compensator (13) to address the uncertainty of friction. The other major source of uncertainty is caused by the arm carrying an unknown payload. The payload estimation algorithm from [27] will be used to improve the controller's performance with unknown payloads. The algorithm requires the parameters  $C_f$ ,  $S_{threshold}$  and  $\tau_{e,threshold}$  to be manually tuned. Note that the payload estimation does not affect the stability of the closed-loop system since it is performed offline (i.e., prior to the position control).

## VII. CONSTRAINED IMPACT MODELLING AND SIMULATION

In this section, dynamic models are developed and used to simulate a constrained impact between a robot arm and a human's head. These models can be used to simulate and compare the safety of electric, pneumatic and hybrid actuators. Since head injuries are the most serious, a constrained impact scenario (where the head is prevented from moving away from the robot) will be studied. In some of the prior robotics literature, the "Head Injury Criterion (HIC)" has been used to assess the injury risk of an impact with human head (e.g. [28]). This criterion is based on the magnitude of

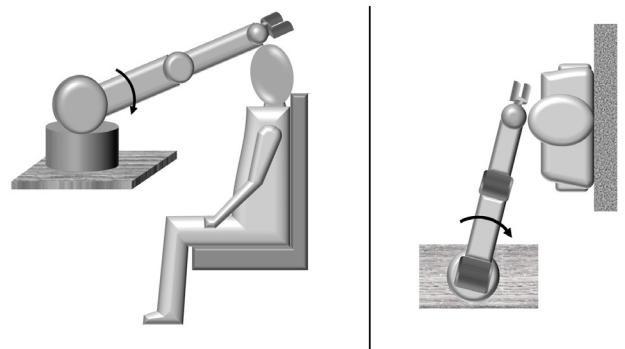


**FIGURE 5.** Illustrations of constrained head-robot impacts for a seated person (left) and standing person (right).

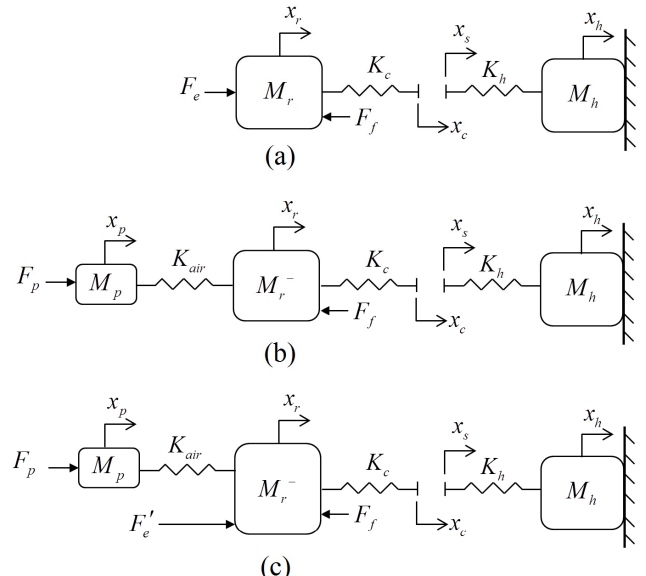


**FIGURE 6.** Impact model schematics for: (a) electric actuator [22], (b) pneumatic actuator and (c) hybrid pneumatic-electric actuator.

head acceleration after the impact. It cannot be used with the constrained impact case studied here since the head doesn't move. Instead, the peak impact force is considered as the safety criterion as in the international standard [29].

Fig. 5 illustrates the impact scenario. A dynamic impact model for this scenario assuming an impact occurring near the arm's tip, arm rotation in the horizontal plane, and an electrically actuated robot was presented in our prior work [22]. It also assumed that the deflection of the joint transmission and the bending of the links were negligible. In the modelling equations all displacements were relative to the head's position,  $x_h$ . The displacements of the arm, compliant cover, skull and pneumatic actuator are termed  $x_r$ ,  $x_c$ ,  $x_s$  and  $x_p$ , respectively.

Two additional models are introduced in this paper to allow the simulation of robots employing pneumatic or hybrid actuators. As in [22], the impact dynamics in the normal direction are modelled by a linear one dimensional lumped parameter model. Fig. 6 shows the new models below the

original model developed for electric actuators. In the new model for the pneumatic actuator, air compliance is modeled as a linear spring acting between the piston position and joint position. The pneumatic model also includes a delay (not shown in the figure) since the pneumatic actuator's force changes relatively slowly. The hybrid impact model has both actuators acting in parallel. As in the original model [22] the electric actuator's delay is assumed to be negligible.

In these models,  $M_h$ ,  $M_r$  and  $M_p$  are head mass, equivalent robot mass, and the equivalent mass of the pneumatic cylinders' pistons and rods, respectively. Also  $M_r^- = M_r - M_p$  and  $K_h$ ,  $K_c$  and  $K_{air}$  are the head equivalent stiffness, robot's compliant cover stiffness, and the equivalent air stiffness for the pneumatic actuator, respectively.  $F_e$ ,  $F_p$  and  $F_f$  are the electric actuator force, pneumatic actuator force, and friction force in the robot joint, respectively. The robot's equivalent mass is calculated from the inertia of the actuator,  $I_{actuator}$ , and inertia of the link,  $I_{link}$ , using:

$$M_r = (I_{actuator} + I_{link}) / d_i^2 \quad (30)$$

where  $d_i$  is the distance from the impact point on the robot to the joint.

The friction force is modelled as the sum of dry and viscous friction components as follows:

$$F_f = \begin{cases} f_k \text{sign}(\dot{x}_r) + k_v \dot{x}_r & \text{if } \dot{x}_r \neq 0 \\ F_{cont} - F_i & \text{if } \dot{x}_r = 0 \wedge |F_{cont} - F_i| < f_s \\ f_s \text{sign}(F_{cont} - F_i) & \text{otherwise.} \end{cases} \quad (31)$$

where  $F_{cont}$  equals  $F_e$ ,  $F_p$  or  $F'_e + F_p$  for the electric, pneumatic and hybrid actuator, respectively;  $f_k$  is the kinetic friction force;  $f_s$  is the static friction force; and  $k_v$  is the coefficient of viscous friction.

Assuming a standard PD plus feedforward controller is used, the electric actuator's force is given by:

$$F_e = \hat{M}_r \ddot{x}_d - K_{P,e}(x_r - x_d) - K_{D,e}(\dot{x}_r - \dot{x}_d) \quad (32)$$

where  $\hat{M}_r$  is the nominal value of  $M_r$ ;  $x_r$  and  $x_d$  are actual and desired positions of the robot arm at the impact point, respectively;  $K_{P,e}$  is the proportional gain; and  $K_{D,e}$  is the derivative gain. The PD gains can be obtained from the desired closed-loop bandwidth,  $f_{bw}$ , and desired damping ratio,  $\zeta$ , as follows:

$$\omega_n = 2\pi f_{bw} / \left( \zeta + \sqrt{1 + \zeta^2} \right), \quad (33)$$

$$K_{P,e} = \hat{M}_r \omega_n^2 \quad \text{and} \quad (34)$$

$$K_{D,e} = 2\zeta \sqrt{K_{P,e} \hat{M}_r} \quad (35)$$

From (12) the desired pneumatic actuator force in the normal direction is:

$$F_{p,d} = \hat{M}_r \ddot{x}_d + \frac{\tau_f^*}{d_i} - K_{PL}(x_r - x_d) - K_{DL}(\dot{x}_r - \dot{x}_d) \quad (36)$$

where  $K_{PL} = K_P/d_i^2$  and  $K_{DL} = K_D/d_i^2$ . The actual pneumatic actuator force is modelled as:

$$F_p(t) = F_{p,d}(t - t_d) \quad (37)$$

where  $t_d$  is the pneumatic actuator's delay.

With the hybrid actuator, the force from the electric motor is obtained from (17) as follows:

$$F'_e = -K_{PLM}(x_r - x_d) - K_{DLM}(\dot{x}_r - \dot{x}_d) \quad (38)$$

where  $K_{PLM} = K_{P,m}/d_i^2$  and  $K_{DLM} = K_{D,m}/d_i^2$ .

For the electric actuator model (Fig. 6-a) the robot's equation of motion is:

$$M_r \ddot{x}_r = F_e - F_f - F_i \quad (39)$$

Here  $F_i$  is the impact force applied to the head by the robot (and vice-versa) through the model's springs, defined by:

$$F_i = \begin{cases} K_{hc} & x_r > 0 \\ 0 & x_r \leq 0 \end{cases} \quad (40)$$

where:

$$K_{hc} = K_h K_c / (K_h + K_c) \quad (41)$$

For the pneumatic actuator (Fig. 6-b), the robot's equation of motion (39) is replaced by (42) and (43).

$$M_r^- \ddot{x}_r = K_{air}(x_p - x_r) - F_f - F_i \quad (42)$$

$$M_p \ddot{x}_p = F_p - K_{air}(x_p - x_r) \quad (43)$$

When the hybrid actuator is used (Fig. 6-c), (42) is replaced by:

$$M_r^- \ddot{x}_r = K_{air}(x_p - x_r) + F_e - F_f - F_i \quad (44)$$

Finally, the equivalent linear stiffness due to air compressibility must be calculated at the impact point. To do this we make the following assumptions:

- Both chambers are assumed to be at the midpoint pressure  $P_{mid} = \frac{1}{2}(P_0 + P_s)$  before the collision.
- The arm's displacement during the impact is small enough to apply local linearization.

Change of volume in each chamber due to the displacement is:

$$dV = A_g r_p dx / d_i \quad (45)$$

where  $dx$  is the displacement at the impact point. The pressure in CG1 after the displacement,  $P'_1$ , is then:

$$P_{mid} V_1 = P'_1 (V_1 + dV) \Rightarrow P'_1 = (V_1 / (V_1 + dV)) P_{mid} \quad (46)$$

Using the same approach:

$$P'_2 = (V_2 / (V_2 - dV)) P_{mid} \quad (47)$$

The air stiffness equation is derived by dividing the pneumatic force equation by the equivalent linear displacement

and linearizing the result. The following equations show the derivation.

$$\begin{aligned} K_{\text{air}} &= (P'_2 - P'_1) A_g / dx \\ &= P_{\text{mid}} A_g (V_2 / (V_2 - dV) - V_1 / (V_1 + dV)) / dx \\ &= P_{\text{mid}} A_g \left( (V_1 + V_2) dV / \left( V_1 V_2 + (V_2 - V_1) dV - dV^2 \right) \right) \end{aligned} \quad (48)$$

Linearizing (48) for  $dV \approx 0$ , substituting  $dV$  from (45) and simplifying gives:

$$\begin{aligned} K_{\text{air}} &= P_{\text{mid}} A_g (V_1 + V_2) dV / V_1 V_2 dx \\ &= P_{\text{mid}} A_g (V_1 + V_2) (A_g r_p dx / d_i) / V_1 V_2 dx \\ &= P_{\text{mid}} A_g^2 r_p (V_1 + V_2) / d_i V_1 V_2 \end{aligned} \quad (49)$$

The impact models for the three actuators have been simulated using Verlet numerical integration. The simulations were programmed in Matlab. They assume  $\hat{M}_r = M_r$  and a zero payload. Table 2 shows the parameters used in the simulations. The controller gains in (32) were chosen such that the electric actuator has the same bandwidth as the electric component of the hybrid actuator, and  $\zeta = 0.7$ . The  $K_{\text{air}}$  value was calculated assuming the impact happens when  $\theta = 90^\circ$ . Note that the value of  $M_h$  is irrelevant due to the head being constrained in the simulations. The electric actuator parameters were obtained from the last column of Table 1. This actuator [25], [26] is almost equivalent to the existing hybrid actuator in terms of maximum continuous output torque. The corresponding maximum controller force of 56.4 N was obtained by dividing the maximum torque by  $d_i$ . The parameters of the pneumatic and hybrid actuators were calculated from the tuned parameters used in the experiments, section VIII.

Fig. 7 shows a comparison result for a robot moving at 0.25 m/s before impact. This speed is the maximum permitted by the international safety standard [31] when a human is within reach of a robot arm. The peak impact forces are 29.9 N, 41.2 N and 63.1 N for the hybrid, pneumatic and electric actuators, respectively. These results show the higher inherent safety of hybrid actuators. Although it has the same bandwidth as the electric component of the hybrid actuator, with the electric actuator the controller force increases fast and saturates. This contributes to the higher impact force caused by the standalone electric actuator. The sudden large increase in the controller force doesn't occur with the hybrid actuator since the ratio of the electric force to the pneumatic force is small. With the  $x_r$  curves for the pneumatic and hybrid cases the arm moves back and loses contact after the first impact, due to their larger compliance. The arm driven by the electric actuator does not lose contact and causes the relatively large skull deflection of 0.42 mm.

## VIII. EXPERIMENTS

For the experiments, a nominal payload mass (not visible in Fig. 3) of 1.4 kg was attached to the end of the 0.7 m arm,

**TABLE 2. Impact simulation parameters.**

Parameter	Value	Description
$d_i$	0.7 m	Distance from the impact point on the robot to the joint
$dt$	0.01 ms	Solver time step
$T_s$	1 ms	Controller sampling period
$K_c$	25 kN/m	Compliant cover stiffness [30]
$K_h$	150 kN/m	Head stiffness [29]
$I_{\text{link}}$	0.068 kgm <sup>2</sup>	Link's moment of inertia
<b>Electric Actuator</b>		
$M_r$	2.0 kg <sup>†</sup>	Equivalent robot mass
$f_k$	4.9 N	Kinetic friction force
$f_s$	4.9 N	Static friction force
$k_v$	0.69 Ns/m	Coefficient of viscous friction
$f_{bw}$	19.4 Hz	Desired closed-loop bandwidth
$K_{P,e}$	7956.1 N/m	Position controller gain
$K_{D,e}$	175.5 Ns/m	Position controller gain
<b>Pneumatic and Hybrid Actuators</b>		
$M_r$	0.18 kg <sup>‡</sup>	Equivalent robot mass
$M_p$	0.052 kg	Equivalent mass of pistons and rods
$K_{\text{air}}$	490 N/m	Air stiffness
$t_d$	5 ms	Pneumatic actuator delay
$f_k$	0.33 N	Kinetic friction force
$f_s$	0.33 N	Static friction force
$k_v$	0.047 Ns/m	Coefficient of viscous friction
$K_{PLM}$	1428.6 N/m	Position controller gain for electric motor
$K_{DLM}$	10.2 Ns/m	Position controller gain for electric motor
$K_{PL}$	1020.4 N/m	Position controller gain for pneumatic actuator
$K_{DL}$	12.2 Ns/m	Position controller gain for pneumatic actuator

<sup>†</sup>. Obtained using (30) and  $I_{\text{actuator}} = 0.90 \text{ kgm}^2$  (see Table I).

<sup>‡</sup>. Obtained using (30) and  $I_{\text{actuator}} = 0.018 \text{ kgm}^2$ . Note that the motor's inertia is only 0.7% of this value.

making the nominal payload's moment of inertia equal to 0.69 kgm<sup>2</sup>. The total rotational inertia is equivalent to a linear actuator translating a 573 kg mass. Tables 3 and 4 list the system parameters and the tuned controller parameters, respectively. The hardware details were presented in section II.

## A. IDENTIFICATION OF INVERSE VALVE MODELS

Identification of the inverse valve models is a prerequisite for implementation of the two pressure control loops.

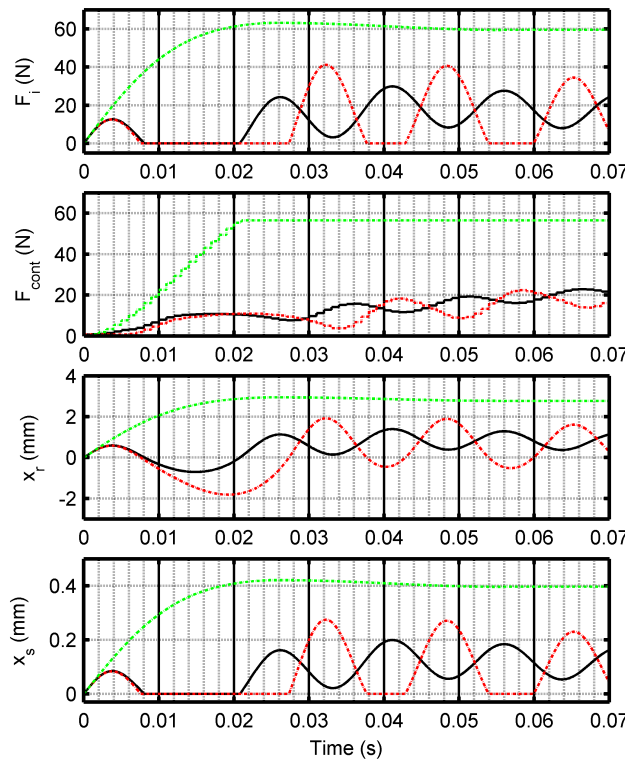


**FIGURE 7.** Impact simulation results for the three actuators, hybrid (black) pneumatic (red) and electric (green). A constrained head-robot impact has been modeled with the robot moving at a constant speed of 0.25 m/s before the impact. The actuators are almost equivalent in terms of maximum continuous output torque.

**TABLE 3.** HPEA system parameters.

Parameter	Value	Description
$I_{total}$	$0.773 \text{ kgm}^2$	Total moment of inertia with nominal payload of 1.40 kg
$r_p$	0.0315 m	Pitch radius of the pinion gear
$A_g$	$0.0022 \text{ m}^2$	Total cross-sectional area of each CG
$V_{01}$	$1.50 \times 10^{-4} \text{ m}^3$	CG1 volume at $\theta = 0$
$V_{02}$	$3.65 \times 10^{-4} \text{ m}^3$	CG2 volume at $\theta = 0$
$d_p$	0.7 m	Distance from axis of rotation to payload's center of mass
$\tau_f^+$	0.2 Nm	Friction model parameter
$\tau_f^-$	-0.5 Nm	Friction model parameter
$P_s$	675 kPa absolute	Supply pressure

The pressure and duty cycle data was acquired using the procedure given in [27]. Next, the coefficients of the polynomials in (20) were calculated using least squares curve fitting. To keep the models parsimonious and avoid overfitting, the model orders were chosen as the smallest values that yielded an acceptable fitting error. The chosen values are  $A = 1$ ,  $B = 3$  and  $G = 3$ . The fit had RMSE values of 3.4%

**TABLE 4.** Tuned controller parameters.

Parameter	Value	Description
$K_P$	500 Nm/rad	Pneumatic position controller gain
$K_D$	6 Nms/rad	Pneumatic position controller gain
$K_{P,m}$	700 Nm/rad	Electric position controller gain
$K_{D,m}$	5 Nms/rad	Electric position controller gain
$K_p'$	$70 \text{ s}^{-1}$	Pressure controller gain
$K_I$	$50 \text{ s}^2$	Pressure controller gain
$\lambda^+$	0.004 Nm	Friction compensator parameter
$\lambda^-$	0.004 Nm	Friction compensator parameter
$\delta$	$8 \times 10^{-5} \text{ rad}$	Friction compensator parameter
$\tau_{f,min}^*$	-1.5 Nm	Friction compensator parameter
$\tau_{f,max}^*$	1.5 Nm	Friction compensator parameter
$C_f$	0.9	Payload estimator parameter
$S_{threshold}$	0.2	Payload estimator parameter
$\tau_{e,threshold}$	0.5 Nm	Payload estimator parameter

and 3.7% for  $u_1$  and  $u_2$ , respectively. Note that these models are different than in [27] due to the higher supply pressure used in this paper (i.e., 675 kPa vs. 480 kPa [27]).

## B. PERFORMANCE OF THE PRESSURE CONTROL LOOPS

The gains of the two inner-loop pressure controllers (21) must be manually tuned before the outer-loop position controller can be implemented. The tuning was performed with the arm fixed at  $\theta = 90^\circ$ . With the arm fixed, a smooth desired pressure trajectory was used with one CG, while the other CG was left open to the atmosphere. This process was then repeated for the other CG. Fig. 8 shows the results of this process for CG1. The pressure tracking resulted in an RMSE of 1.90 kPa (0.3% of  $\max(P_{1d})$ ) and Maximum Absolute Error (MaxAE) of 5.1 kPa (0.8%) averaged over five experiments. Similar RMSE and MaxAE values were obtained with CG2. Fig. 8 also shows that the control signal,  $u_1$ , is fairly smooth and does not saturate.

## C. PERFORMANCE OF THE POSITION CONTROL

A multi-cycloidal trajectory similar to that used in [6] was tested next. Example results are plotted in Fig. 11. The pneumatic torque,  $\tau_p$ , was calculated using the measured pressures and (2). The electric torque,  $\tau_m$ , was calculated using  $u_m$  and (9). These torques will be discussed later. A slower multi-cycloidal trajectory similar to that used in [20] has also been used for this experiment to facilitate comparison. Tracking small moves can be a challenge for servo systems due to

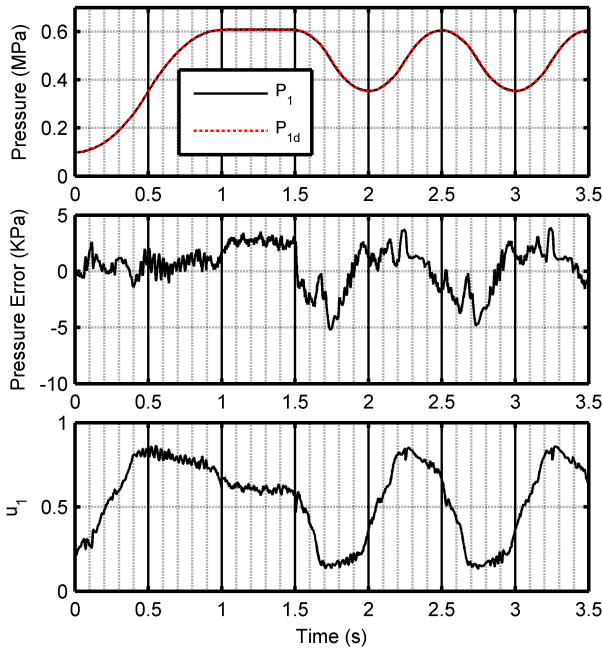


**FIGURE 8.** Experimental pressure control result for CG1.

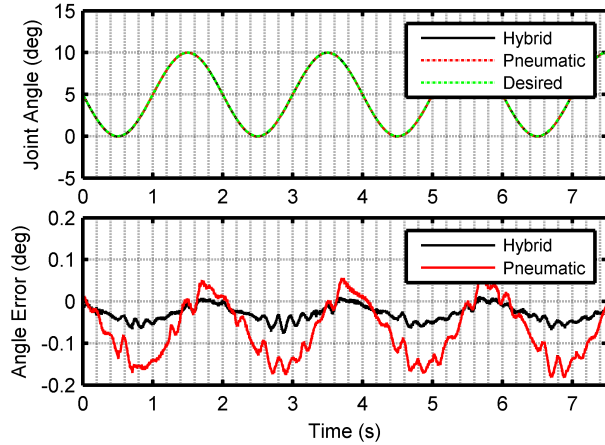


**FIGURE 9.** Experimental position control results for 0.5 Hz sinusoidal desired trajectory.

stiction effects. Thus a  $0.045^\circ$  move has been added to the multi-cycloidal trajectory to further challenge the position controller and friction compensator.

This move has been added to the  $90^\circ$  section where the gravity torque is near its maximum. Fig. 12 shows the overall results and Fig. 13 shows a magnified view of the small move. It can be seen that both actuators are responsive to the  $0.045^\circ$  change in trajectory. The pneumatic actuator shows some overshoot tendency in positive direction movements but the electric motor successfully removes the overshoot for the hybrid case. The observed SSE for both actuators was less than or equal to the encoder resolution i.e.  $0.0045^\circ$ . Comparing the torque plots in Figs. 11 and 12, it can be observed that the electric motor's contribution is much smaller with the slower trajectory in Fig. 12. The reason is the pneumatic

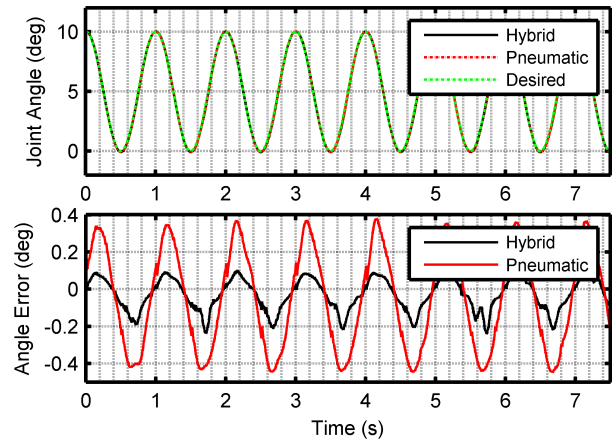


**FIGURE 10.** Experimental position control results for 1 Hz sinusoidal desired trajectory.

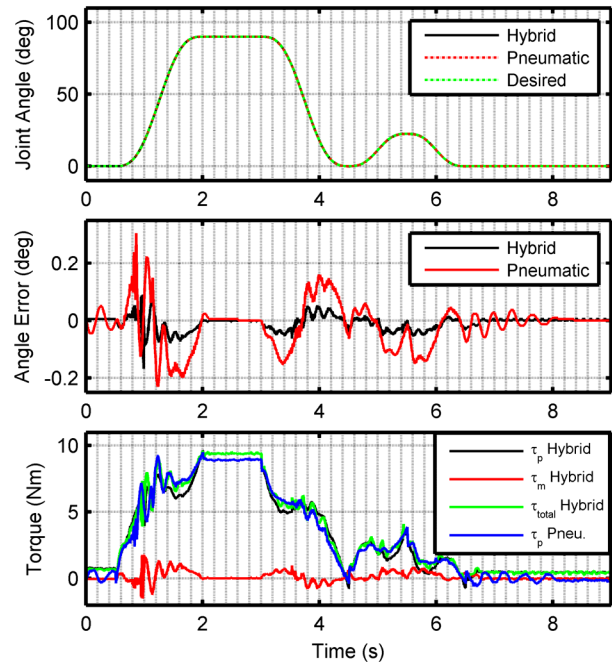


**FIGURE 11.** Experimental position control results when tracking the fast multi-cycloidal trajectory.  $\tau_{total} = \tau_p + \tau_m$  is the total torque for the hybrid actuator.

actuator was fast enough to supply most of the required torque with the slower trajectory, but with the fast trajectory more of the fast torque from the motor was necessary. Experiments were performed five times for each trajectory. The maximum absolute error (MaxAE) and RMSE values were calculated and averaged. Table 5 lists the averaged results. In this table, the 0.5 Hz sinusoidal trajectory, 1 Hz sinusoidal trajectory experiment, fast multi-cycloidal trajectory, and slow multi-cycloidal trajectory with  $0.045^\circ$  move are numbered 1-4, respectively.

With trajectories 1, 2 and 3 a similar large RMSE reduction was observed when the hybrid actuator was used instead of the pneumatic one (64.6%, 65.6% and 67.6%, respectively).

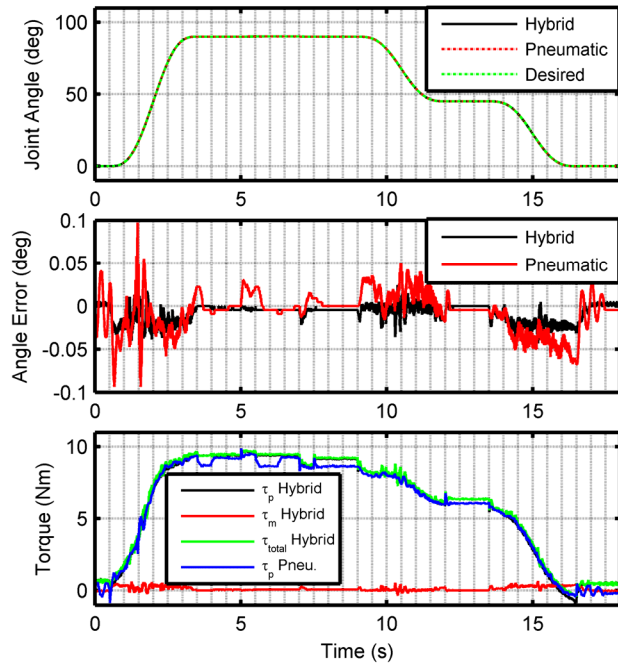


**FIGURE 12.** Experimental position control results for the pneumatic and hybrid actuators tracking the slower multi-cycloidal trajectory containing a  $0.045^\circ$  move.  $\tau_{\text{total}} = \tau_p + \tau_m$  is the total torque for the hybrid actuator.

**TABLE 5.** Position control experimental results.

Trajectory No.	Pneumatic Actuator		Hybrid Actuator	
	RMSE	MaxAE	RMSE	MaxAE
1	$0.096^\circ$	$0.194^\circ$	$0.034^\circ$	$0.077^\circ$
2	$0.273^\circ$	$0.454^\circ$	$0.094^\circ$	$0.252^\circ$
3	$0.074^\circ$	$0.305^\circ$	$0.024^\circ$	$0.167^\circ$
4	$0.023^\circ$	$0.097^\circ$	$0.012^\circ$	$0.043^\circ$

For trajectory 4 this RMSE reduction was 55.7%. The reason for smaller reduction was the use of a slower trajectory which was less challenging for the pneumatic actuator. The hybrid actuator also reduced the MaxAE by 60.3%, 44.5%, 45.2%, and 55.7% for trajectories 1 to 4, respectively.

#### D. ROBUSTNESS TO UNKNOWN PAYLOADS

To evaluate the robustness of the control system to unknown payloads, the controller parameters were fixed and two different payloads were used. The first produced a 53% decrease in payload inertia relative to its nominal value, while the second produced a 34.7% increase in relative inertia. In Fig. 14, example experimental results are shown for the tracking errors with, and without, the payload estimator. A multiple cycloidal trajectory identical to the one in Fig. 11 was used for these tests. The results of the various test conditions are presented in Table 6. These values were obtained by averaging the RMSE and MaxAE values from five experiments performed at each test condition. They clearly demonstrate that improved position tracking was obtained when the offline payload estimator was used.

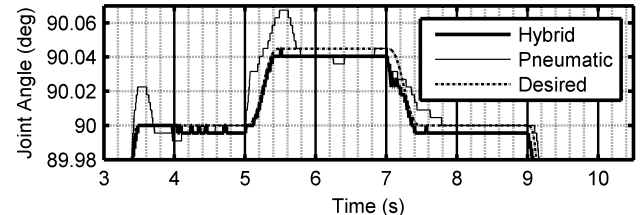


**FIGURE 13.** Magnified view of the results for a  $0.045^\circ$  move.

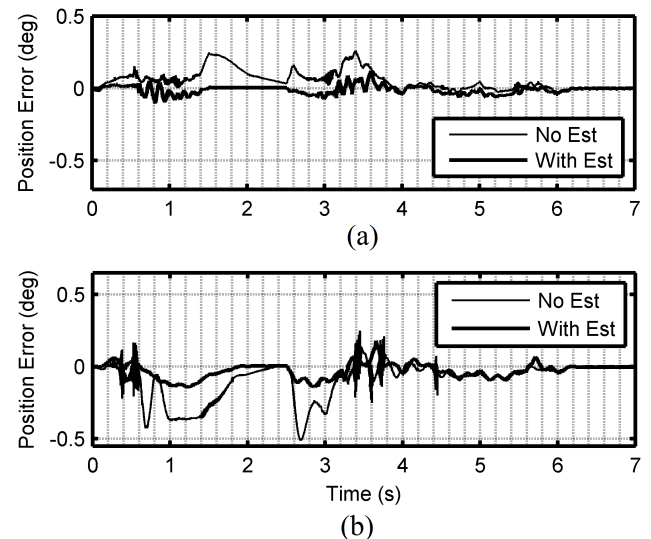


**FIGURE 14.** Tracking errors for unknown payload experiments with and without using the payload estimator for: (a) lower-than-nominal payload, and (b) higher-than-nominal payload.

**TABLE 6.** Payload robustness experimental results.

Payload	Estimator Status	RMSE (deg)	MaxAE (deg)
Nominal	Off	0.024	0.167
Light (-53.0%)	Off	0.076	0.262
(-53.0%)	On	0.027	0.121
Heavy (+34.7%)	Off	0.139	0.513
(+34.7%)	On	0.052	0.178

#### E. COMPARISON WITH STATE OF THE ART

The best performances for a position controlled high torque pneumatic rotary actuator and position controlled HPEA were reported in [6] and [20], respectively. In [6] the SSE of the pneumatic actuator for a trajectory similar to trajectory 3 was about  $2^\circ$ , compared to  $0.0045^\circ$  in this paper. The RMSE of  $4^\circ$  from [6] was 53 times larger. Compared to the pneumatic actuator results in [27], the RSME with trajectory 3 was reduced by 56% (i.e.,  $0.074^\circ$  vs.  $0.169^\circ$ ). For the HPEA with similar hardware used in [20], the RMSE reported for trajectory 4 were  $0.096^\circ$  and  $0.038^\circ$  for the pneumatic and hybrid actuators, respectively. Thus the use of the model-based pressure controller and improved friction compensator in this paper has led to RMSE reductions of 76% and 68.4% for the pneumatic and the hybrid actuator, respectively.

## IX. CONCLUSION

In this paper a new HPEA design is presented with significantly higher torque output than previous designs, while maintaining the low mechanical impedance and inherent safety of the HPEA approach. This design is cost efficient since it does not require a high precision gearbox or harmonic drive to connect the motor to the output shaft, and uses solenoid on/off valves rather than costly proportional/servo valves. The HPEA is controlled by two inner-loop pressure controllers and an outer-loop position controller. The accuracy of the empirical inverse valve model enabled the pressure controllers to achieve high performance. Based on numerous experiments, the combination of adaptive friction compensation, model-based feedforward compensation, feedback compensation and offline payload estimation allowed the HPEA to outperform the state of the art in terms of position RMSE and SSE. Dynamic models were developed for a constrained impact between a human head and robot arm powered by either the HPEA, a pneumatic actuator, or a conventional electric actuator. The simulation results showed that the HPEA produced the smallest impact force. The proposed HPEA can provide future collaborative robot arms with precise positioning, better inherent safety than conventional actuators, and lower production cost.

## REFERENCES

- [1] M. Zinn, B. Roth, O. Khatib, and J. K. Salisbury, "A new actuation approach for human friendly robot design," *Int. J. Robot. Res.*, vol. 23, nos. 4–5, pp. 379–398, 2004.
- [2] A. K. Paul, J. E. Mishra, and M. G. Radke, "Reduced order sliding mode control for pneumatic actuator," *IEEE Trans. Control Syst. Technol.*, vol. 2, no. 3, pp. 271–276, Sep. 1994.
- [3] X. Shen, J. Zhang, E. J. Barth, and M. Goldfarb, "Nonlinear model-based control of pulse width modulated pneumatic servo systems," *ASME J. Dyn. Syst., Meas., Control*, vol. 128, no. 3, pp. 663–669, 2006.
- [4] T. Nguyen, J. Leavitt, F. Jabbari, and J. E. Bobrow, "Accurate sliding-mode control of pneumatic systems using low-cost solenoid valves," *IEEE/ASME Trans. Mechatronics*, vol. 12, no. 2, pp. 216–219, Apr. 2007.
- [5] S. Hodgson, M. Tavakoli, M. T. Pham, and A. Leleve, "Nonlinear discontinuous dynamics averaging and PWM-based sliding control of solenoid-valve pneumatic actuators," *IEEE/ASME Trans. Mechatronics*, vol. 20, no. 2, pp. 876–888, Apr. 2015.
- [6] J. E. Bobrow and B. W. McDonell, "Modeling, identification, and control of a pneumatically actuated, force controllable robot," *IEEE Trans. Robot. Autom.*, vol. 14, no. 5, pp. 732–742, Oct. 1998.
- [7] M. A. Azman, A. A. M. Faudzi, M. O. Elnimair, O. F. Hikmat, K. Osman, and C. C. Kai, "P-adaptive neuro-fuzzy and PD-fuzzy controller design for position control of a modified single acting pneumatic cylinder," in *Proc. IEEE/ASME Int. Conf. Adv. Intel. Mechatronics*, Jul. 2013, pp. 176–181.
- [8] R. A. Rahman, L. He, and N. Sepehri, "Design and experimental study of a dynamical adaptive backstepping-sliding mode control scheme for position tracking and regulating of a low-cost pneumatic cylinder," *Int. J. Robust Nonlinear Control*, vol. 26, no. 4, pp. 853–875, 2015.
- [9] C.-K. Chen and J. Hwang, "Iterative learning control for position tracking of a pneumatic actuated X-Y table," *Control Eng. Pract.*, vol. 13, pp. 1455–1461, Dec. 2005.
- [10] Z. Rao and G. M. Bone, "Nonlinear modeling and control of servo pneumatic actuators," *IEEE Trans. Control Syst. Technol.*, vol. 16, no. 3, pp. 562–569, May 2008.
- [11] R. B. van Varseveld and G. M. Bone, "Accurate position control of a pneumatic actuator using on/off solenoid valves," *IEEE/ASME Trans. Mechatronics*, vol. 2, no. 3, pp. 195–204, Sep. 1997.
- [12] L. J. Petrosky, "Hybrid electro-pneumatic robot joint actuator," U.S. Patent 4 782 258, Oct. 28, 1987.
- [13] F. Takemura, S. R. Pandian, Y. Nagase, H. Mizutani, Y. Hayakawa, and S. Kawamura, "Control of a hybrid pneumatic/electric motor," in *Proc. IEEE/RSJ Int. Conf. Intell. Robots Syst.*, Oct./Nov. 2000, pp. 209–214.
- [14] D. Shin, I. Sardellitti, and O. Khatib, "A hybrid actuation approach for human-friendly robot design," in *Proc. IEEE Int. Conf. Robot. Autom.*, May 2008, pp. 1747–1752.
- [15] G. M. Bone and X. Chen, "Position control of hybrid pneumatic-electric actuators," in *Proc. Amer. Control Conf.*, 2012, pp. 1793–1799.
- [16] T. Teramae, T. Noda, S.-H. Hyon, and J. Morimoto, "Modeling and control of a pneumatic-electric hybrid system," in *Proc. IEEE/RSJ Int. Conf. Intell. Robots Syst.*, vol. 4, no. 8, Nov. 2013, pp. 4887–4892.
- [17] Y. Nakata, T. Noda, J. Morimoto, and H. Ishiguro, "Development of a pneumatic-electromagnetic hybrid linear actuator with an integrated structure," in *Proc. IEEE/RSJ Int. Conf. Intell. Robots Syst.*, Sep./Oct. 2015, pp. 6238–6243.
- [18] K. Ishihara and J. Morimoto, "An optimal control strategy for hybrid actuator systems: Application to an artificial muscle with electric motor assist," *Neural Netw.*, vol. 99, pp. 92–100, Mar. 2018.
- [19] G. M. Bone, M. Xue, and J. Flett, "Position control of hybrid pneumatic-electric actuators using discrete-valued model-predictive control," *Mechatronics*, vol. 25, pp. 1–10, Feb. 2015.
- [20] G. Ashby and G. M. Bone, "Improved hybrid pneumatic-electric actuator for robot arms," in *Proc. IEEE Int. Conf. Adv. Intell. Mechatronics*, Banff, AB, Canada, Jul. 2016, pp. 100–106.
- [21] J. F. Carneiro and F. G. de Almeida, "Modeling pneumatic servovalves using neural networks," in *Proc. IEEE Conf. Comput. Aided Control Syst. Design*, Munich, Germany, Oct. 2006, pp. 790–795.
- [22] B. Rouzbeh and G. M. Bone, "Impact force reduction strategies to achieve safer human-robot collisions," in *Proc. CSME Int. Congr.*, Toronto, ON, Canada, 2018, pp. 1–5.
- [23] S. Davis and D. G. Caldwell, "Braid effects on contractile range and friction modeling in pneumatic muscle actuators," *Int. J. Robot. Res.*, vol. 25, no. 4, pp. 359–369, 2006.
- [24] Universal Robots. (2015). *Max. Joint Torques—17260*. [Online]. Available: <http://www.universal-robots.com/how-tos-andfaqs/faq/ur-faq/max-joint-torques-17260/>
- [25] *A465 Robot Arm User Guide*, CRS Robot., Burlington, ON, Canada, 2000.
- [26] *Torquemaster Brush Servo Motors 3500 Series Characteristics*, Cleveland Motion Controls, Cleveland, OH, USA, 2002.
- [27] B. Rouzbeh, G. M. Bone, and G. Ashby, "High-accuracy position control of a rotary pneumatic actuator," *IEEE/ASME Trans. Mechatronics*, vol. 23, no. 6, pp. 2774–2781, Dec. 2018, doi: [10.1109/TMECH.2018.2870177](https://doi.org/10.1109/TMECH.2018.2870177).
- [28] M. Van Damme, B. Vanderborght, B. Verrelst, R. Van Ham, F. Daerden, and D. Lefever, "Proxy-based sliding mode control of a planar pneumatic manipulator," *Int. J. Robot. Res.*, vol. 28, no. 2, pp. 266–284, 2009.
- [29] *Robots and Robotic Devices—Collaborative Robots*, Standard ISO/TS 15066:2016, International Organization for Standardization, 2016.
- [30] L. Zeng and G. M. Bone, "Design of elastomeric foam-covered robotic manipulators to enhance human safety," *Mech. Mach. Theory*, vol. 60, pp. 1–27, Feb. 2013.
- [31] *Robots for Industrial Environments—Safety Requirements—Part I: Robot*, Standard ISO 10218-1:2011, International Organization for Standardization, 2011.



**BEHRAD ROUZBEH** received the B.S. and M.S. degrees in mechanical engineering from the Amirkabir University of Technology, Iran, in 2009 and 2013, respectively.

He is currently pursuing the Ph.D. degree in mechanical engineering with McMaster University, Hamilton, ON, Canada, where he is currently a Lecturer. His research interests include the control of dynamic systems, hybrid robotic actuators, and collaborative robots.



**GARY M. BONE** received the B.Sc. (Ap.Sc.) degree in mechanical engineering from Queen's University, Canada, and the M.Eng. and Ph.D. degrees in mechanical engineering from McMaster University, Canada, in 1986, 1988, and 1993, respectively.

He joined the Faculty of Engineering, McMaster University, in 1994, where he is currently a Professor with the Department of Mechanical Engineering. His current research interests include robot design and control, servo pneumatic actuators, hybrid actuators, collaborative robots, and soft robots.



**EUGENE LI** received the B.A.Sc. degree in mechatronics and the M.A.Sc. degree in electrical engineering from the University of Waterloo, Canada, in 2012 and 2014, respectively.

He is currently pursuing the part-time Ph.D. degree in mechanical engineering with McMaster University, Canada. He is currently with the University of Waterloo, Canada. His current research interests include soft robotics and collaborative robotics.

• • •



**GRAHAM ASHBY** received the B.Eng. degree and the M.A.Sc. degree in mechanical engineering from McMaster University, Canada, in 2012 and 2015, respectively.

He is currently involved in the field of laboratory instrument automation with Mantech Canada, Guelph, ON, Canada.